Tuning the magnetic interactions in van der Waals Fe 3 GeTe 2 heterostructures: A comparative study of ab initio methods

Dongzhe Li, Soumyajyoti Haldar, Tim Drevelow, Stefan Heinze

Tuning the magnetic interactions in van der Waals Fe_3GeTe_2 heterostructures: A comparative study of *ab initio* methods

Dongzhe Li [1,*] Soumyajyoti Haldar [2] Tim Drevelow [2] and Stefan Heinze [2,3]
[1]*CEMES, Université de Toulouse, CNRS, 29 rue Jeanne Marvig, F-31055 Toulouse, France*
[2]*Institute of Theoretical Physics and Astrophysics, University of Kiel, Leibnizstrasse 15, 24098 Kiel, Germany*
[3]*Kiel Nano, Surface, Interface Science (KiNSIS), University of Kiel, Kiel, Germany*

(Received 27 October 2022; revised 13 February 2023; accepted 14 March 2023; published 29 March 2023)

We investigate the impact of mechanical strain, stacking order, and external electric fields on the magnetic interactions of a two-dimensional (2D) van der Waals heterostructure in which a 2D ferromagnetic metallic Fe_3GeTe_2 monolayer is deposited on germanene. Three distinct computational approaches based on *ab initio* methods are used, (i) the Green's function method, (ii) the generalized Bloch theorem, and (iii) the supercell approach, and a careful comparison is given. First, the shell-resolved exchange constants are calculated for the three Fe atoms within the unit cell of the freestanding Fe_3GeTe_2 monolayer. We find that the results obtained with approaches (i) and (ii) are in good qualitative agreement and also in good qualitative agreement with previously reported values. An electric field of $\mathcal{E} = \pm 0.5$ V/Å applied perpendicular to the Fe_3GeTe_2/germanene heterostructure leads to significant changes in the exchange constants. We show that the Dzyaloshinskii-Moriya interaction (DMI) in Fe_3GeTe_2/germanene is mainly dominated by the nearest neighbors, resulting in a good quantitative agreement between approaches (i) and (ii). Furthermore, we demonstrate that the DMI is highly tunable by strain, stacking, and electric field, leading to a large DMI comparable to that of ferromagnetic/heavy metal interfaces, which have been recognized as prototypical multilayer systems to host isolated skyrmions. The geometrical change and hybridization effect explain the origin of the high tunability of the DMI at the interface. The electric-field-driven DMI obtained by approach (iii) is in qualitative agreement with the more accurate *ab initio* method used in approach (ii). However, the field effect on the DMI is overestimated by approach (iii) by about 50%. This discrepancy is attributed to the different implementations of the electric field and basis sets used in the *ab initio* methods applied in approaches (ii) and (iii). The magnetocrystalline anisotropy energy (MAE) can also be drastically changed by the application of compressive or tensile strain in the Fe_3GeTe_2/germanene heterostructure. The application of an electric field, in contrast, leads only to relatively small changes in the MAE for electric fields of up to 1 V/Å.

DOI: 10.1103/PhysRevB.107.104428

I. INTRODUCTION

Magnetic skyrmions [1]—topologically protected chiral spin structures with particlelike properties—have attracted tremendous attention due to their potential application in next-generation spintronics devices such as racetrack memories [2], logic gates [3], artificial synapses for neuromorphic computing [4], and qubits for quantum computing [5]. The formation of magnetic skyrmions is due to the competition between the Heisenberg exchange and Dzyaloshinskii-Moriya interaction (DMI) [6–9] together with the magnetocrystalline anisotropy energy (MAE). In particular, the DMI plays an essential role in stabilizing skyrmions since it favors canted spin configurations with a unique rotational sense. The DMI results from spin-orbit coupling and is only nonzero for systems with broken inversion symmetry. Magnetic skyrmion lattices were discovered in experiments on bulk chiral magnets [10,11] and in epitaxial ultrathin films [12]. Isolated magnetic skyrmions were observed in ultrathin transition-metal films at low temperatures [13–15] and at room temperature in magnetic multilayers [16–19], in ferrimagnets [20], and in synthetic antiferromagnets [21].

Recently, long-range magnetism was reported in two-dimensional (2D) materials [22–24]. This provides a promising alternative avenue for exploring topological spin structures in atomically thin layers. Several recent experiments reported the observation of skyrmions in 2D van der Waals (vdW) heterostructures, such as at an Fe_3GeTe_2/WTe_2 interface [25], in an Fe_3GeTe_2/Co/Pd multilayer [26], and at a $Cr_2Ge_2Te_6/Fe_3GeTe_2$ interface [27]. Moreover, magnetic domain walls [28] and nonreciprocal magnons [29] were reported in the Fe_3GeTe_2 surface. The origin of skyrmions in these systems was attributed to the interfacial DMI. A comprehensive material survey has been done by *ab initio* calculations to explore the DMI in 2D magnets. The family of monolayer Janus vdW magnets has been predicted to possess large enough DMI to allow stable skyrmions [30–35]. Néel-type magnetic skyrmions were also observed in Fe_3GeTe_2 crystals and were attributed to the DMI due to oxidized interfaces [36]. In addition, it has been proposed that skyrmions can be stabilized in 2D vdW multiferroic heterostructures [37],

*dongzhe.li@cemes.fr

in moiré structures of vdW 2D magnets [38], and even in centrosymmetric materials [39] induced by exchange frustration. For most 2D magnets, the DMI is absent due to inversion symmetry. It is possible to break the inversion symmetry by designing various 2D vdW heterostructures and applying an electric field, or strain [40,41]. This indicates the possibility of tuning DMI via external stimuli in 2D vdW heterostructures.

From the theoretical point of view, the calculation of the DMI at the *ab initio* level is, in principle, relatively straightforward, nevertheless, complications can arise in practice. Several approaches have been introduced based on different first-principles methods and used by numerous groups to calculate the DMI for various material classes [9,30,42–53]: unfortunately, mostly without a sufficient cross-check between them. This invites a detailed benchmark study to validate different approaches; however, so far this has only been performed for the ultrathin-film system of a Co monolayer on Pt(111) [54]. Such comparative studies are crucial to understanding the origin of skyrmion stability, particularly for the newly discovered 2D magnets.

Here, using *ab initio* calculations, we compare systematically three current state-of-the-art approaches to extract magnetic interaction parameters in heterostructures based on Fe_3GeTe_2 (FGT), namely, (i) by the Green's function method [55], (ii) by using the generalized Bloch theorem (gBT) [43,54,56,57], or (iii) by using the supercell approach [49]. First we study the shell-resolved exchange interaction between the Fe atoms of the different layers in a freestanding FGT monolayer. We find that approaches (i) and (ii) are in good qualitative agreement. We then focus on the structural and magnetic properties of the 2D vdW heterostructure of an FGT monolayer deposited on germanene under strain, stacking, and an electric field. We find that a small compressive strain γ of about 3% can significantly enhance the DMI in FGT heterostructures by more than 400% compared with the value without strain. The variation of the DMI is mainly due to the geometrical change of the FGT monolayer. Such a large DMI is comparable to that in state-of-the-art ferromagnetic/heavy metal (FM/HM) heterostructures, which have been demonstrated as prototypical multilayer systems to host individual skyrmions even at room temperature. Furthermore, the DMI can be substantially modified via different stacking geometry due to the hybridization effect at the interface.

Upon applying an electric field, the strength of the DMI varies almost linearly and can even change sign when a strong electric field ($\mathcal{E} > 1$ V/Å) is applied. The exchange constants are also considerably modified due to an electric field while the effect on the magnetocrystalline anisotropy energy (MAE) is small. However, the MAE is dramatically reduced to 25% of its original value at a compressive strain of $\gamma = -3\%$. In connection with the exchange frustration in FGT/germanene, these large changes in the DMI and MAE open the possibility of zero-field magnetic skyrmions [58]. For the DMI in FGT/Ge, the three theoretical approaches are in good qualitative agreement, and we also discuss the quantitative comparison in detail.

The paper is organized as follows. In Sec. II, we describe the three theoretical approaches used to obtain the relevant spin-spin interaction parameters by mapping the *ab initio* density functional theory (DFT) calculations onto an extended Heisenberg model. In Sec. III, we examine the Heisenberg exchange for freestanding FGT followed by the DMI and MAE for FGT heterostructures. Different theoretical approaches are carefully benchmarked. We further investigate the effects of biaxial strain, stacking configuration, and an electric field on the magnetic interactions in FGT heterostructures. Finally, we summarize our main conclusions in Sec. IV.

II. METHODS AND COMPUTATIONAL DETAILS

In order to describe the magnetic properties of FGT heterostructures, we use the extended Heisenberg model for the spins of Fe atoms in the hexagonal structure:

$$H = -\sum_{ij} J_{ij}(\mathbf{m}_i \cdot \mathbf{m}_j) - \sum_{ij} \mathbf{D}_{ij} \cdot (\mathbf{m}_i \times \mathbf{m}_j) - \sum_{i} K_i \left(m_i^z\right)^2, \quad (1)$$

where $\mathbf{m}_i$ and $\mathbf{m}_j$ are normalized magnetic moments at positions $\mathbf{R}_i$ and $\mathbf{R}_i$, respectively. The three magnetic interaction terms correspond to the Heisenberg isotropic exchange, the DMI, and the MAE, respectively, and they are characterized by the parameters J_{ij}, $\mathbf{D}_{ij}$, and K_i in the related terms. Note that by using Eq. (1) it is assumed that the magnetic moments are constant.

During the past decade, in order to obtain the parameters very accurately in Eq. (1), several approaches have been developed based on density functional theory (DFT), which is frequently named the *ab initio* atomistic spin model. In this paper, we apply three different approaches for the calculation of magnetic interactions in FGT vdW heterostructures: (i) the Green's function method [55,59] (also known as the Liechtenstein formula) employing infinitesimal rotations; (ii) the generalized Bloch theorem (gBT) [56], which allows one to calculate the total energy of spin spirals of any wave vector $\mathbf{q}$ in magnetic nanostructures [57]; and (iii) the supercell approach [49], which is straightforward but computationally heavy due to the comparison of total energies in a supercell geometry. We performed DFT calculations using two community *ab initio* codes which differ in their choice of basis set: The QUANTUMATK (QATK) package [60] uses an expansion of electronic states in a linear combination of atomic orbitals (LCAO), while the FLEUR code [61] is based on the full-potential linearized augmented plane wave (FLAPW) formalism. The former is computationally very efficient, while the latter ranks amongst the most accurate implementations of DFT. In the following, we denote the three different approaches as LCAO-Green, FLAPW-gBT, and LCAO-supercell for simplicity. Apart from the methods presented above, there are also other approaches widely used in the community for calculations of spin-spin interactions, e.g., the four-state method [62] and the machine learning approach [63].

A. The Green's function method: LCAO-Green

For the variation of total energy due to the spin interactions in Eq. (1), we obtain the following variation with respect to $\mathbf{m}_i$

and $\mathbf{m}_j$:

$$\delta E_{ij} = -2J_{ij}(\delta\mathbf{m}_i \cdot \delta\mathbf{m}_j) - 2\delta\mathbf{m}_i\underline{\mathbf{J}}_{ij}^{\mathrm{ani}}\delta\mathbf{m}_j - 2\mathbf{D}_{ij} \cdot (\delta\mathbf{m}_i \times \delta\mathbf{m}_j), \quad (2)$$

where the first term represents the isotropic exchange (i.e., Heisenberg exchange) and the second term is the the symmetric anisotropic exchange, where $\underline{\mathbf{J}}_{ij}^{\mathrm{ani}}$ is a 3×3 symmetric tensor. The last term corresponds to the DMI.

The Green's function method treats the local rigid spin rotation as a perturbation. Using the force theorem, the total energy variation due to the two-spin interaction between sites i and j is

$$\delta E_{ij} = -\frac{2}{\pi}\int_{-\infty}^{E_{\mathrm{F}}} dE\ \mathrm{Im\ Tr}[\delta\underline{\mathbf{H}}_{ii}\underline{\mathbf{G}}_{ij}\delta\underline{\mathbf{H}}_{jj}\underline{\mathbf{G}}_{ji}], \quad (3)$$

where $\underline{\mathbf{H}}_{ii} = \delta\mathbf{e}_i \cdot \boldsymbol{\sigma}$ and $\underline{\mathbf{G}}_{ij} = G_{ij}^0\underline{\mathbf{I}} + \mathbf{G}_{ij} \cdot \boldsymbol{\sigma}$ are the real-space Hamiltonian and the Green's function.[1] Here, $\mathbf{e}_i = \mathbf{m}_i$ is a unit orientation vector (normalized to 1).

Then, in Eq. (3), if we take the trace in both orbital (L) and spin space ($\boldsymbol{\sigma}$), we end up with the following expression:

$$\begin{aligned}\mathrm{Tr}_{L,\sigma}[\delta\underline{\mathbf{H}}_{ii}\underline{\mathbf{G}}_{ij}\delta\underline{\mathbf{H}}_{jj}\underline{\mathbf{G}}_{ji}] &= -2\left[G_{ij}^0G_{ji}^0 - \sum_{\mu\in(x,y,z)}\underline{\mathbf{G}}_{ij}^{\mu}\underline{\mathbf{G}}_{ji}^{\mu}\right]\delta\mathbf{e}_i\delta\mathbf{e}_j \\ &- 2\sum_{\mu,\nu\in(x,y,z)}\delta\mathbf{e}_i^{\mu}\left(\underline{\mathbf{G}}_{ii}^{\mu}\underline{\mathbf{G}}_{ji}^{\nu} + \underline{\mathbf{G}}_{ij}^{\mu}\underline{\mathbf{G}}_{ji}^{\nu}\right)\delta\mathbf{e}_j^{\nu} \\ &- 2\mathbf{D}_{ij} \cdot (\delta\mathbf{e}_i \times \delta\mathbf{e}_j). \end{aligned} \quad (4)$$

To simplify for the notation of Eq. (4), we define a central quantity for the Green's function method, namely, the $\underline{\mathbf{A}}$ matrix, which has a 4×4 size as follows:

$$A_{ij}^{\mu\nu} = -\frac{1}{4\pi}\int_{-\infty}^{E_{\mathrm{F}}} dE\ \mathrm{Tr}_L\left[\underline{\mathbf{G}}_{ij}^{\mu}\underline{\mathbf{G}}_{ji}^{\nu}\right], \quad (5)$$

where indices μ and ν run over 0, x, y, or z.

Finally, comparing Eq. (4) with Eq. (2), the Heisenberg exchange and the DMI can be expressed by using only the $\mathbf{A}$ matrix as follows:

$$J_{ij} = 2\ \mathrm{Im}\left(A_{ij}^{00} - A_{ij}^{xx} - A_{ij}^{yy} - A_{ij}^{zz}\right)\frac{\underline{\mathbf{\Delta}}_{ii}\underline{\mathbf{\Delta}}_{jj}}{4}, \quad (6)$$

$$J_{ij}^{\mathrm{ani}} = 2\ \mathrm{Im}\left(A_{ij}^{\mu\nu} + A_{ij}^{\nu\mu}\right)\frac{\underline{\mathbf{\Delta}}_{ii}\underline{\mathbf{\Delta}}_{jj}}{4}, \quad (7)$$

$$\mathbf{D}_{ij}^{\mu} = 2\mathrm{Re}\left(A_{ij}^{0\mu} - A_{ij}^{\mu 0}\right)\frac{\underline{\mathbf{\Delta}}_{ii}\underline{\mathbf{\Delta}}_{jj}}{4}, \quad (8)$$

[1]Throughout this paper, vectors are denoted with bold characters, while matrices are represented by bold plus single underline (e.g., $\underline{\mathbf{G}}_{ij}$). Moreover, L represents the orbital index, while $\boldsymbol{\sigma} = (\sigma_x, \sigma_y, \sigma_z)$ is the spin index.

where $\underline{\mathbf{\Delta}}_{ii} = (\underline{\mathbf{H}}_{ii}^{\uparrow} - \underline{\mathbf{H}}_{ii}^{\downarrow})$ is the on-site difference between the spin-up and spin-down parts of the Hamiltonian matrix.

If we neglect spin-orbit coupling (SOC), the DMI vanishes, $\underline{\mathbf{G}}^x = \underline{\mathbf{G}}^y = 0$, $\underline{\mathbf{G}}^0 = 1/2(\underline{\mathbf{G}}^{\uparrow} + \underline{\mathbf{G}}^{\downarrow})$, $\underline{\mathbf{G}}^z = 1/2(\underline{\mathbf{G}}^{\uparrow} - \underline{\mathbf{G}}^{\downarrow})$, and we arrive at the original Liechtenstein-Katsnelson-Antropov-Gubanov (LKAG) formula [55] which was proposed in 1987,

$$J_{ij} = -\frac{1}{4\pi}\int_{-\infty}^{E_{\mathrm{F}}} dE\ \mathrm{Im\ Tr}[\underline{\mathbf{\Delta}}_{ii}\underline{\mathbf{G}}_{ij}^{\uparrow}\underline{\mathbf{\Delta}}_{jj}\underline{\mathbf{G}}_{ji}^{\downarrow}], \quad (9)$$

where $\underline{\mathbf{G}}_{ij}$ becomes Hermitian.

Note that the derivations above are general for orthogonal and nonorthogonal basis sets. Please refer to Ref. [64] for a detailed demonstration within the nonorthogonal basis set.

Our Green's function calculations were performed using QATK [60] in two steps: (i) We performed LCAO-DFT calculations with SOC in order to construct the tight-binding-like Hamiltonian matrix $\mathbf{H}_{ij}$ and the overlap matrix $\mathbf{S}_{ij}$. (ii) The magnetic exchange parameters were evaluated as described above by Eqs. (3)–(9). For LCAO-DFT calculations on FGT monolayers and on FGT/Ge heterostructures, the energy cutoff for the density grid sampling was set to 150 hartrees, and a 28×28 $\mathbf{k}$-point mesh was adopted for the Brillouin zone (BZ) integration. For magnetic exchange calculations, we used a much denser $\mathbf{k}$-point mesh of 48×48, 60 circle contour points, and 13th-nearest neighbors in order to obtain accurate numerical integration. Using these parameters, we extracted J_{ij} and $\mathbf{D}_{ij}$ parameters with an accuracy of 0.01 meV. Note that this approach, i.e., infinitesimal spin rotations, fits well to magnetic skyrmions, in which we often have large noncollinear spin structures.

B. The generalized Bloch theorem: FLAPW-gBT

The second approach employs the FLAPW method as implemented in the FLEUR code [61] and is based on the generalized Bloch theorem (gBT) [56,57]. It allows one to consider spin spirals of any wave vector $\mathbf{q}$ for systems without SOC. We first self-consistently compute within the scalar-relativistic approximation the energy dispersion, $E_{\mathrm{SS}}(\mathbf{q})$, of homogeneous flat spin spirals [57] which are characterized by a wave vector $\mathbf{q}$ and an angle $\phi = \mathbf{q} \cdot \mathbf{R}$ between adjacent magnetic moments separated by lattice vector $\mathbf{R}$.

As a second step, the DMI is computed within first-order perturbation theory on the self-consistent spin spiral state [43,46,54]. The energy variation $\delta\epsilon_{\mathbf{k},\nu}(\mathbf{q})$ of these states due to the SOC Hamiltonian can be written as

$$\delta\epsilon_{\mathbf{k},\nu}(\mathbf{q}) = \langle\Psi_{\mathbf{k},\nu}(\mathbf{q})|\, H_{\mathrm{SOC}}\, |\Psi_{\mathbf{k},\nu}(\mathbf{q})\rangle\,, \quad (10)$$

where $|\Psi_{\mathbf{k},\nu}(\mathbf{q})\rangle$ are the self-consistent solutions in the scalar-relativistic approximation, $\mathbf{k}$ is the Bloch vector, and ν is the band index. By integration over the Brillouin zone and summation over all occupied bands ν, this gives the total energy contribution for spin spirals due to SOC denoted as $E_{\mathrm{DMI}}(\mathbf{q})$.

We map the energy dispersion in the scalar-relativistic approximation, $E_{\mathrm{SS}}(\mathbf{q})$, and the energy contribution to spin spirals due to DMI, $E_{\mathrm{DMI}}(\mathbf{q})$, to the atomistic spin model, Eq. (1), in order to extract the exchange constants, J_{ij}, and the magnitudes of $\mathbf{D}_{ij}$, respectively. One of the key advantages of

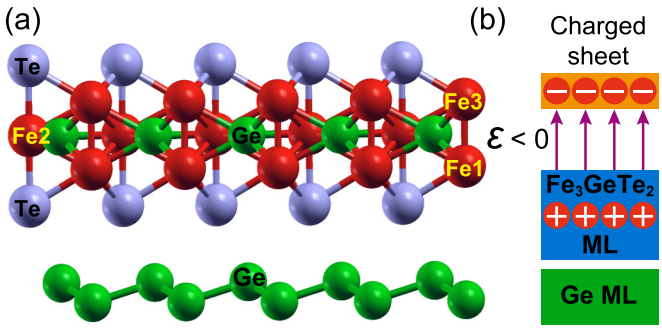

FIG. 1. (a) Sketch of the studied 2D magnetic vdW heterostructure of an Fe_3GeTe_2 monolayer (ML) on germanene. Three nonequivalent Fe atoms are indicated as red spheres: Fe1 (bottom, interface atom), Fe2 (middle atom), and Fe3 (top atom). Te and Ge atoms are given by gray and green spheres, respectively. (b) The electric field is created by a charged sheet located at 5.3 Å above the FGT. The direction of electric field lines for $\mathcal{E} < 0$ is shown.

the gBT approach is that even incommensurate spin spirals and those with a large **q** can be treated very efficiently in the chemical unit cell, i.e., without the need for large supercells.

We used a cutoff parameter for the FLAPW basis functions of $k_{\max} = 4.0$ a.u.$^{-1}$, and we included basis functions including spherical harmonics up to $l_{\max} = 8$. The muffin tin radii used for Fe, Ge, and Te are 2.10, 2.10, and 2.63 a.u., respectively. Moreover, we treated $3s$, $3p$, and $4d$ states by local orbitals for Fe and Te, respectively. To extract the J_{ij} and $\mathbf{D}_{ij}$ parameters, we converge the total energy of flat spin spiral states (without SOC and with one-shot SOC) using a 33×33 **k**-point mesh. For conical spin spiral calculations, we increased the **k**-point mesh up to 49×49 since the energy dispersion amplitude is much smaller than for the flat ones. We model the effect of a uniform electric field by placing a charged sheet in the vacuum region of FGT/Ge (see Fig. 1), i.e., using the same methodology and sign convention of the electric field as in Ref. [65]. We maintain the charge neutrality of the whole system by adding or removing the same amount of opposite charge to or from the interface. Finally, we computed the MAE using the force theorem using a denser **k** mesh of 64×64.

C. The supercell approach: LCAO-supercell

In this approach, the DMI within the nearest-neighbor approximation for a specific system is calculated from the energy difference between a clockwise (CW) and a counterclockwise (CCW) 90° spin spiral calculated within a supercell. $d_\parallel$ can be obtained by the following formula [49]:

$$d_\parallel = (E_{\mathrm{CCW}} - E_{\mathrm{CW}})/8\sqrt{3}. \tag{11}$$

The corresponding micromagnetic DMI coefficient D is given by

$$D = \frac{3\sqrt{2}d_\parallel}{N_{\mathrm{FM}}a^2}, \tag{12}$$

where a and N_{FM} are the lattice constant and number of ferromagnetic layers, respectively.

Note that by varying the supercell size one can go beyond the nearest-neighbor DMI approximation. However, the computational effort is much larger than using the spin spiral approach sketched above.

We used the QATK code [60] and a 4×1 supercell where first-neighbor spins rotated as 90°. A 7×28 **k**-point mesh was adopted for the BZ integration. We included the effect of SOC self-consistently. Although the supercell approach is straightforward and SOC can be treated self-consistently, it is limited to only very large wave vectors.

III. RESULTS AND DISCUSSION

Throughout this paper, we use the following conventions. We use a minus sign in the Heisenberg exchange terms [cf. Eq. (1)], meaning that $J_{ij} > 0$ ($J_{ij} < 0$) favors ferromagnetic (antiferromagnetic) alignment between moments $\mathbf{m}_i$ and $\mathbf{m}_j$. For the DMI constants, a positive (negative) sign denotes a preferred CW (CCW) rotational sense. In addition, without specification, we give in this paper the in-plane component of the DMI since the out-of-plane component has been shown to be negligible forming skyrmions in 2D magnets [30,66]. All effective quantities, such as the Heisenberg exchange, the DMI, and the MAE, are measured in meV/unit cell. Note that there are three Fe atoms per unit cell of FGT (Fig. 1).

A. Geometric properties

We consider FGT heterostructures in which an FGT monolayer is deposited on germanene (denoted as FGT/Ge in the following). As shown in Fig. 1(a), FGT adopts the space group (194) $P6_3/mmc$ and can be seen from the perspective of the atomistic spin model as a stack of three Fe hexagonal layers in hcp stacking. In the following, the top, center, and bottom (interface) atoms are denoted as Fe3, Fe2, and Fe1, respectively.

The motivation behind the use of germanene as a nonmagnetic layer is as follows. We recently demonstrated that the buckled structure of germanene could enhance the structural asymmetry of FGT under strain [58]. More importantly, such an efficient strain-driven DMI control is general for FGT heterostructures with buckled substrates (e.g., silicene and antimonene). On the other hand, in experiments, FGT/graphene [67], and FGT/hBN [68] have been synthesized. Since germanene is very similar to graphene in many aspects, the FGT/Ge interface is expected to be feasible.

We have used the QATK code with plane-wave basis sets for the atomic relaxation. We employed the generalized gradient approximation (GGA), obtaining a relaxed lattice constant of 4.00 Å for the Fe_3GeTe_2 monolayer, which is in good agreement with experimental data ranging between about 3.991 and 4.03 Å [69,70]. Then, germanene is matched at the interface with FGT with a lattice mismatch smaller than 1%. The structures were fully relaxed until the energy and the forces on each atom were less than 10^{-8} Ry and 10^{-4} Ry/bohr, respectively. We also took into account van der Waals interactions using semiempirical dispersion corrections as formulated by Grimme *et al.* [71]. We used the local density approximation (LDA) for the magnetic calculations with LCAO basis sets. We did not take into account the Hubbard U correction

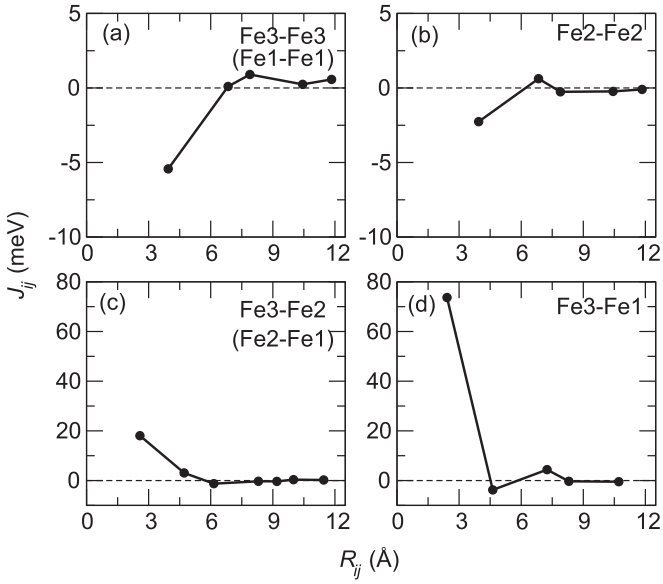

FIG. 2. Calculated Heisenberg exchange constants as a function of distance R_{ij} between sites i and j for a freestanding FGT monolayer obtained within the LCAO-Green approach. (a) and (b) Intralayer exchange interactions for Fe3-Fe3 (Fe1-Fe1) and Fe2-Fe2 spin pairs, respectively. (c) and (d) Interlayer exchange interactions for Fe3-Fe2 (Fe2-Fe1) and Fe3-Fe1 spin pairs, respectively. Note that $J_{ij} > 0$ and $J_{ij} < 0$ correspond to favored ferromagnetic and antiferromagnetic alignment. The distances are given in Ångströms.

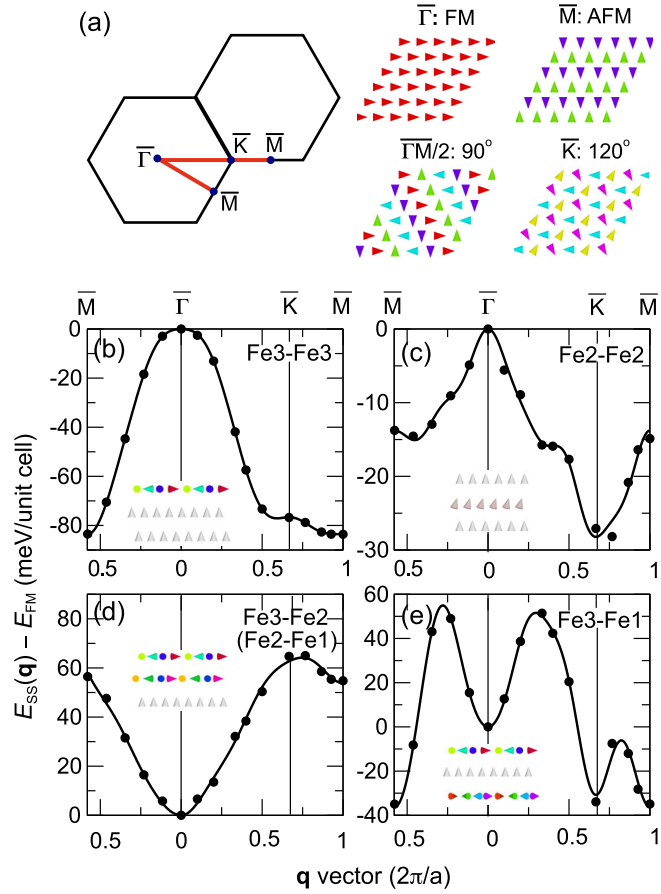

FIG. 3. Energy dispersions of spin spirals without SOC for freestanding FGT using the FLAPW-gBT approach. (a) Sketches of the 2D hexagonal Brillouin zone and of the FM state ($\overline{\Gamma}$ point), the row-wise AFM state ($\overline{M}$ point), the 90° spin spiral (at $\overline{\Gamma M}/2$), and the Néel state with 120° between adjacent spins ($\overline{K}$ point). (b) and (c) Intralayer spin spirals for Fe3-Fe3 and Fe2-Fe2 spin pairs, respectively. (d) and (e) Interlayer spin spirals for Fe3-Fe1 and Fe3-Fe2 spin pairs, respectively. All energies are given relative to the energy of the FM state, E_{FM}. Black points are from FLAPW-gBT calculations, and the dispersion curve is obtained by fitting the FLAPW-gBT data to the Heisenberg model (up to seventh-nearest neighbors). Insets show the spin spiral configurations in the three Fe layers of FGT used to determine the given Fe-Fe interactions. Note that to determine the Fe2-Fe2 exchange, we used conical spin spirals in the Fe2 layer [see inset of (c)] and rescaled the energy dispersion (see text for details).

since the LDA yields a magnetic moment of 1.76 μ_B/Fe that compares well with experiments, as previously pointed out in Refs. [24,72]. It has been shown recently by Ghosh *et al.* that using DFT+U leads to a less favorable description of the magnetic properties for the FGT family [73]. The lowest-energy stacking configuration is the one where the Te atom is right above the center of the hexagonal ring of germanene with an optimized vdW gap of about 2.86 Å [see Fig. 1(b)], which agrees well with previous results [74].

B. Freestanding FGT monolayer: Heisenberg exchange

Let us first consider the Heisenberg pairwise exchange in the freestanding FGT monolayer (Fig. 2). Here, due to the lack of broken inversion symmetry, Fe3 and Fe1 are equivalent. Therefore we end up with four different spin pairs, {Fe3-Fe3 (equivalently Fe1-Fe1), Fe2-Fe2} and {Fe2-Fe1 (equivalently Fe3-Fe2), Fe3-Fe1}, sorted by intra- and interlayer exchange interactions. We show in Fig. 2 the Heisenberg exchange constants J_{ij} with respect to distance R_{ij} computed by the Green's function method. All J_{ij} decrease quickly with distance, some showing an oscillatory character. The intralayer interactions [Figs. 2(a) and 2(b)] favor antiferromagnetic (AFM) coupling with moderate strength of the nearest-neighbor exchange constants $J^1_{\text{Fe3-Fe3}} = -5.43$ meV and $J^1_{\text{Fe2-Fe2}} = -2.26$ meV, while the interlayer exchange [Figs. 2(c) and 2(d)] favors much stronger ferromagnetic (FM) coupling with $J^1_{\text{Fe3-Fe1}} = 73.16$ meV and $J^1_{\text{Fe2-Fe1}} = 18.08$ meV. In particular, the competition between FM and AFM pairs yields geometric frustration in a triangular sublattice, which can help to stabilize noncollinear spin structures [75–78]. Clearly, the most significant exchange coupling originates from the interaction between Fe3 and Fe1 atoms, which are on top of each other (cf. Fig. 1). It drops quickly to a small negative value, i.e., AFM coupling, at the second-nearest distance and goes up again to a small positive value at the third-nearest distance [Fig. 2(d)]. Similar results have been reported for FGT bulk [79].

In order to quantitatively compare the results presented above with different DFT approaches, we have calculated the exchange constants also by the FLAPW-gBT method. In Fig. 3, we present the energy dispersions $E_{ss}(\mathbf{q})$ of homogeneous spin spirals (per unit cell) for a freestanding FGT monolayer. The energy dispersions are calculated in

the scalar-relativistic approximation, i.e., neglecting SOC, along the high-symmetry directions $\overline{\Gamma M}$ and $\overline{\Gamma KM}$ of the two-dimensional (2D) hexagonal Brillouin zone (BZ). The high-symmetry points represent special states: The $\overline{\Gamma}$ point corresponds to the FM state, the $\overline{M}$ point corresponds to the row-wise AFM state, the $\overline{\Gamma M}/2$ point corresponds to the 90° spin spiral, and the $\overline{K}$ point corresponds to the Néel state with 120° between adjacent spins [Fig. 3(a)].

We focus first on intralayer exchange interactions. To extract only the Fe3-Fe3 exchange parameter, we rotate only Fe3 spins by fixing the Fe2 and Fe1 layers to the FM state [inset of Fig. 3(b)]. The lowest energy for spin spirals in the Fe3 layer is at the $\overline{M}$ point [Fig. 3(b)], indicating an AFM Fe3-Fe3 coupling in good agreement with corresponding LCAO-Green calculations [cf. Fig. 2(a)]. The FM state ($\overline{\Gamma}$ point) is about 83 meV/Fe atom higher in energy.

In the case of the Fe2-Fe2 pair, the direct calculation of flat spin spiral curves propagating only in the Fe2 layer is technically unfeasible due to the complete quenching of the magnetic moment on the Fe2 atom due to symmetry (for details, see Appendix B). This shows that the magnetic moment of Fe2 is only induced by the magnetic moments of Fe1 and Fe3 in the ferromagnetic state. Therefore we used conical spin spirals with a small cone angle of $\theta = 10°$, i.e., close to the FM state, and transformed the obtained energy dispersion back to a flat spin spiral: $E_{\text{flat}}(\mathbf{q}) = E_{\text{coned}}(\mathbf{q})/\sin^2\theta$. As shown in Fig. 3(c), the energy dispersion $E_{\text{flat}}(\mathbf{q})$ for the Fe2 layer becomes qualitatively different compared with the Fe3 layer: The ground state is found to be at the $\overline{K}$ point (Néel state). The energy difference between the FM state and the Néel state is much smaller than in the case of Fe3-Fe3, resulting in a weaker AFM Fe2-Fe2 coupling (see Table III in Appendix A).

To calculate the interlayer exchange interaction, i.e., between Fe3 and Fe2 atoms, we rotate the spins of the Fe3 and Fe2 layers simultaneously by fixing the Fe1 atom to the FM state [Fig. 3(d)]. Then, we remove the intralayer contribution by calculating $E(\mathbf{q}) = E_{\text{Fe3-Fe2}}(\mathbf{q}) - E_{\text{Fe3-Fe3}}(\mathbf{q}) - E_{\text{Fe2-Fe2}}(\mathbf{q})$ (not shown). The FM state at the $\overline{\Gamma}$ point turns out to be the state of lowest energy, and the dispersion $E(\mathbf{q})$ rises quickly for spin spirals with increasing $\mathbf{q}$, resulting in a strong FM coupling which is consistent with the LCAO-Green result [see Fig. 2(c)].

In contrast, the energy dispersion of spin spirals propagating only in the Fe1 and Fe3 layers looks very different [Fig. 3(e)]. The energy minimum is located at the $\overline{M}$ point, and two maxima are observed in the $\overline{\Gamma M}$ and $\overline{\Gamma K}$ directions, indicating an AFM coupling. At first glance, this seems like a qualitative difference between this result and the result of a strong ferromagnetic Fe3-Fe1 coupling observed in the LCAO-Green calculation [Fig. 2(d)]. However, this is due to the fact that the Fe3 and Fe1 atoms are on top of each other and are not distinguishable by spin spirals which propagate in plane with respect to the Fe layers. As a result, if we fit the spin spiral curve in Fig. 3(d), we obtain the shell-resolved exchange constants between the Fe3 and Fe1 atoms, i.e., J_2, J_3, J_4, etc., except for the nearest-neighbor term, J_1, which arises from direct Fe3-Fe1 coupling. To include J_1 explicitly, we have performed an additional calculation with an AFM coupling between the Fe3 and Fe1 atoms.

TABLE I. Comparison of the calculated Heisenberg exchange constants (in meV) for freestanding FGT using the LCAO-Green, the FLAPW-gBT, and the VASP-ML approach (see Ref. [80]). The NN intralayer (Fe3-Fe3 and Fe2-Fe2) and interlayer exchange (Fe3-Fe1 and Fe3-Fe2) constants are presented. The spin moments are the averaged magnetic moments, which are given in μ_B.

	Fe3-Fe3	Fe2-Fe2	Fe3-Fe1	Fe3-Fe2	M_s/Fe
LCAO-Green	−5.43	−2.26	73.16	18.08	1.79
FLAPW-gBT	−10.21	−2.02	83.47	16.50	1.76
VASP-ML [80]	−13.4	−5.1	74.1	39.4	1.66

After that, by comparing the total energies between FM and AFM states, we can obtain J_1 by counting the number of nearest-neighbor atoms, $E_{\text{AFM}}^{\text{Fe3-Fe1}} - E_{\text{FM}}^{\text{Fe3-Fe1}} = 2J_1 + 12(J_2 + J_3 + J_4 + J_6 + J_7) + 24J_5$. The obtained value for the nearest-neighbor Fe3-Fe1 coupling is $J_1 = 83.47$ meV, showing a strong FM coupling as expected. All values for the calculated magnetic interactions up to the seventh-nearest neighbors are given in Appendix A.

Our main results on the exchange constants obtained by the two computational approaches are summarized in Table I. For comparison, the results from a machine learning approach (denoted as VASP-ML, where VASP is the Vienna *ab initio* simulation package) calculated by Xu *et al.* [80] are also included. For simplicity, we compare for all Fe-Fe pairs only the nearest-neighbor (NN) exchange constant. LCAO-Green, FLAPW-gBT, and VASP-ML data are in excellent qualitative agreement. Quantitatively, LCAO-Green yields exchange parameters very close to the corresponding FLAPW-gBT calculation. In particular, the Fe2-Fe2 pairs agree surprisingly well (−2.26 as compared with −2.02 meV), which indicates that the conical spin spirals used in FLAPW-gBT are very close to the Green's function method (FM state).

However, between the exchange constants given here and those given by Xu *et al.* [80] there is a non-negligible discrepancy. In particular, the values for Fe2-Fe2 and Fe3-Fe2 pairs are about 50% higher than those in our FLAPW-gBT results. Reasons for this quantitative discrepancy may be the different lattice constants and different relaxations of atomic positions. Moreover, such a discrepancy might be related to the rather large higher-order exchange interactions (HOIs) which have been obtained for the monolayer of FGT in Ref. [80]. Note that the energy dispersions of spin spirals include implicitly contributions from HOIs which are effectively mapped to our calculated exchange constants as discussed in detail in Ref. [81]. Finally, we note that DFT+U [82] significantly underestimates the exchange parameters for the FGT monolayer compared with our DFT level calculations.

C. FGT/Ge: Dzyaloshinskii-Moriya interaction

We now turn our discussion to the DMI, which plays a central role in the emergence of noncollinear spin structures such as magnetic skyrmions. The DMI originates from SOC, and it only exists in materials lacking inversion symmetry. According to Moriya's symmetry rules [6], since the FGT has a (001) mirror plane, $\mathbf{D}_{ij}$ for each pair of NN Fe atoms is perpendicular to their bonds [83]. Therefore $\mathbf{D}_{ij}$ can be

expressed as

$$\mathbf{D}_{ij} = d_{\parallel}\,(\hat{\mathbf{u}}_{ij}\times\hat{\mathbf{z}}) + d_{\perp}\hat{\mathbf{z}} \tag{13}$$

with $\hat{\mathbf{u}}_{ij}$ being the unit vector between sites i and j and $\hat{\mathbf{z}}$ indicating normal to the plane.

The in-plane component of the DMI constant in the NN approximation, $d_{\parallel}$, can be directly obtained from the supercell approach [49] [see Eq. (11)]. The perpendicular component, $d_{\perp}$, does not play a significant role in 2D magnets, as reported in Refs. [30,66], and is thus neglected. In the following, without specification, our calculated DMI refers to the in-plane DMI component, and $d_{\parallel} > 0$ ($d_{\parallel} < 0$) denotes a CCW (CW) rotational sense.

For freestanding FGT, the DMI involving either Fe1 or Fe3 has opposite signs (i.e., chirality) because of the (001) mirror plane. Upon incorporating germanene in FGT, the inversion symmetry breaking at the FGT/Ge interface gives rise to an emergent DMI. Since the DMI is a key ingredient for the formation of skyrmions, methods for efficiently controlling and manipulating the DMI are essential for designing novel functional spintronics devices. We will show in the following three ways for tuning the DMI in FGT/Ge.

1. Strain

Strain engineering is one of the most commonly used methods to tune the properties of 2D layers. We study the strain-dependent DMI in FGT/Ge. The in-plane biaxial strain is defined as

$$\gamma = (a - a_0)/a_0, \tag{14}$$

where a and a_0 are the strained and unstrained lattice constants of the FGT, respectively. For tensile strain ($\gamma > 0$), the in-plane lattice tends to increase, while for compressive strain ($\gamma < 0$) the in-plane lattice exhibits a decreasing trend.

The calculated microscopic $d_{\parallel}$ and micromagnetic D of the DMI for FGT/Ge are shown in Fig. 4. The DMI is evaluated quantitatively by calculating the self-consistent total energy of cycloidal 90° spin spirals with opposite rotational sense, namely, using the supercell approach (i.e., LCAO-supercell). Both compressive and tensile strains are considered ranging from −3 to 6.25%. Note that FGT has been demonstrated to be stable under such strain via DFT phonon spectrum calculations [84]. We emphasize that the value of $a_0 = 4.0$ Å used in this paper was evaluated by the GGA and is slightly larger than the lattice constant calculated by the LDA, $a_0 = 3.91$ Å. If we use the latter as a reference, the largest compressive strain used in this paper becomes less than −1%. At equilibrium ($\gamma = 0\%$), we find a moderate DMI of about $d_{\parallel} = -0.25$ meV, favoring a CW spin rotation. Its corresponding micromagnetic DMI coefficient is about $|D| = 0.36$ mJ/m^2. This value is comparable to that of the two FGT heterostructures: FGT/In_2Se_3 [85] (∼0.28 mJ/m^2) and FGT/$Cr_2Ge_2Te_6$ [27] (∼0.31 mJ/m^2), which were demonstrated recently as promising vdW heterostructures to stabilize skyrmions.

Even more interestingly, we find a significant increase in the DMI when a small compressive strain is applied (Fig. 4). The extracted $|D|$ is about 1.5 mJ/m^2 at $\gamma = -3\%$, which is comparable to the value previously estimated in FM/HM thin-film systems [12,18,47,49]. Such a large DMI indicates

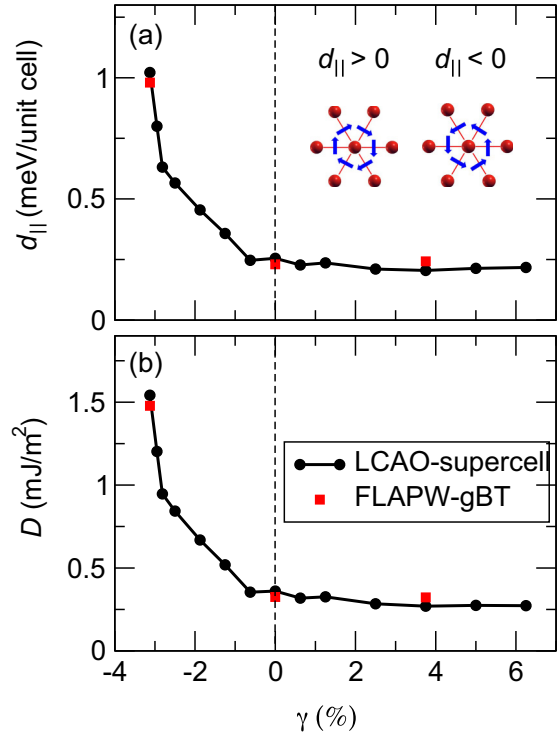

FIG. 4. (a) Microscopic and (b) micromagnetic DMI coefficients in a monolayer FGT on germanene as a function of biaxial strain, γ, obtained by the LCAO-supercell (solid black circles) and FLAPW-gBT (solid red squares) approaches. The inset in (a) shows sketches of the hexagonal Fe layers, the DMI vectors, and the sign convention.

that the FGT/Ge heterostructure can be a promising interface for stable isolated skyrmions [58]. A more detailed analysis shows that the enhancement of the DMI in FGT/Ge is mainly mediated by the geometrical change due to the buckled structure of germanene (see Sec. III C).

The results presented above are reproduced by FLAPW-gBT if we calculate the effective DMI from spin spiral calculations including SOC (red squares in Fig. 4). Here, the effective DMI constant is obtained from fits in the region of low $|\mathbf{q}|$ around the FM state ($\overline{\Gamma}$ point) where the energy contribution due to SOC varies linearly with $|\mathbf{q}|$. Interestingly, the DMI predicted by the LCAO-supercell method is in excellent quantitative agreement with the one calculated by FLAPW-gBT, showing that the reported results are robust against different approaches used. This indicates a possibility of strain control of magnetic skyrmions in these systems. In contrast, a tensile strain ($\gamma > 0$) has almost no effect on the DMI (Fig. 4).

To gain further insight into the local decomposition of the DMI, we show in Fig. 5 the calculated DMI using the LCAO-Green approach for six possible Fe pairs in FGT/Ge as a function of distance with and without strain. Evidently, the external compressive strain ($\gamma = -3\%$) has a significant effect on the DMI of the FGT monolayer, particularly for pairs connected to the interface Fe1 atom. When the strain is applied, a strong enhancement of the DMI favoring a CW (i.e., positive sign) rotational sense is clearly observed for Fe1-Fe1 and Fe2-Fe1 pairs [Figs. 5(c) and 5(f)], indicating

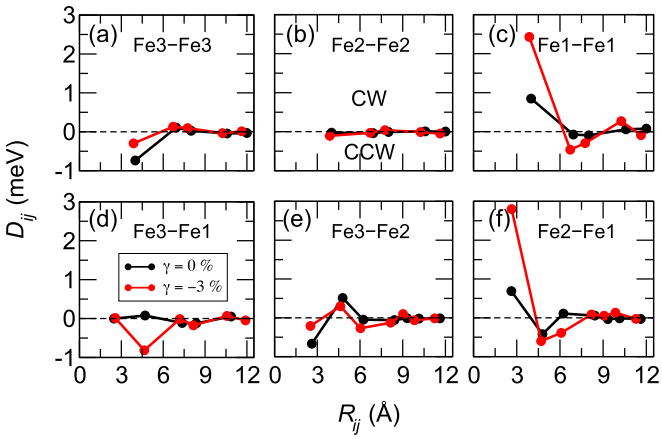

FIG. 5. The DMI parameters D_{ij} between different pairs of Fe atoms as a function of distance for FGT/Ge at $\gamma = 0\%$ (black) and $\gamma = -3\%$ (red), calculated by LCAO-Green. (a)–(c) Intralayer and (d)–(f) interlayer DMI constants are presented. The positive and negative signs denote CCW and CW chirality, respectively.

a strong modification of electronic and magnetic properties at the interface. This is also reflected by the projected density of states in FGT/Ge (see Fig. 11 in Appendix C).

Quantitatively, the nearest-neighbor DMI changes from 0.88 (0.72) to 2.46 (2.84) meV for the Fe1-Fe1 (Fe2-Fe1) pair. A similar behavior is also observed for the second-nearest-neighbor DMI in Fe3-Fe1 [Fig. 5(d)]. The DMI changes from 0.1 to −0.80 meV, accompanying a sign change. On the other hand, Fe3-Fe3 and Fe3-Fe2 interactions [Figs. 5(a) and 5(e)] are much less affected by the strain. Moreover, due to symmetry, the DMI in Fe2-Fe2 [Fig. 5(b)] and the nearest-neighbor Fe3-Fe1 (on top of each other) are almost quenched. These results are also in agreement with those obtained by the TB2J code [86] which uses a similar methodology.

2. Stacking

To study the effect of stacking order on the DMI of the FGT/Ge heterostructure, three fully optimized representative stacking geometries are considered here (see sketches in Fig. 6): (i) stacking 1 (the most favorable stacking geometry), in which the Te atom is right above the center of the hexagonal ring of germanene, (ii) stacking 2, in which the Ge atom of FGT is located above the center of the hexagonal ring of germanene, and (iii) stacking 3, in which the Fe1 and Fe3 atoms of FGT are placed directly above the center of the hexagonal ring of germanene.

Figure 6(a) shows the variation of the DMI strength $d_\parallel$ with respect to strain for these three stacking geometries. We observe a similar behavior for stackings 1 and 2 for the range of γ between about −2 and 6%, namely, a clear enhancement of DMI at compressive strain ($\gamma < 0$) and a nearly constant value for a tensile strain ($\gamma > 0$). Interestingly, when $\gamma < -2\%$, the DMI increases for stacking 1, while it decreases for stacking 2.

To understand the origin of the variation of the DMI, we plot in Figs. 6(b) and 6(c) the geometrical change by strain. As a negative strain is applied, $\Delta z_1 - \Delta z_2$ increases rapidly for both stacking 1 and stacking 2, where Δz_1 and Δz_2 denote the

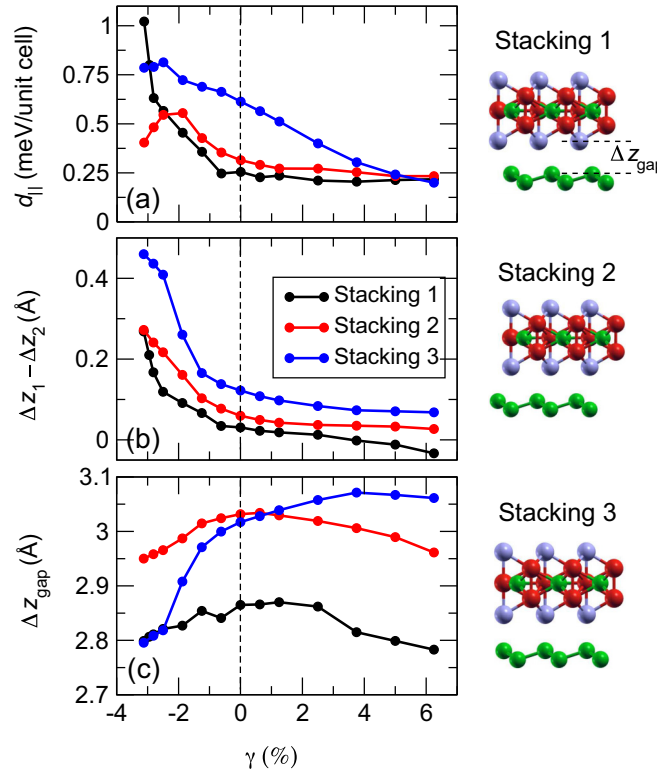

FIG. 6. (a) Stacking-dependent DMI constant in the NN approximation, $d_\parallel$, in FGT/Ge heterostructures obtained by LCAO-supercell. The three types of stacking considered are displayed on the right (see text for details). (b) Strain dependence of $\Delta z_1 - \Delta z_2$ calculated from the Fe1-Fe2 vertical distance, Δz_1, and the Fe2-Fe3 vertical distance, Δz_2. (c) Strain dependence of the van der Waals gap Δz_{gap} (see sketch of stacking 1).

vertical distances between Fe1-Fe2 and Fe2-Fe3. This leads to an increase in the degree of structural asymmetry, resulting in an enhancement of the DMI. On the other hand, the vdW gap induced by hybridization is decreased by strain and is more pronounced for stacking 2 than for stacking 1. As analyzed in detail in Ref. [58], the hybridization effect for FGT/Ge decreases the DMI. This explains why the DMI for stacking 2 is smaller than that for stacking 1 for $\gamma < -2\%$.

For stacking 3, we observe the most pronounced geometrical changes, and the variation of $\Delta z_1 - \Delta z_2$ and of Δz_{gap} is almost two times and three times larger than for stacking 1, respectively. As a result, even at $\gamma = 0\%$ the DMI for stacking 3 is about −0.63 meV, which is 2.5 times higher than the corresponding DMI in stacking 1. However, only a slight increase of the DMI up to about −0.78 meV is observed with compressive strain. Herein, the increase in $d_\parallel$ is mainly due to the interplay between the increase in $\Delta z_1 - \Delta z_2$ and the decrease in Δz_{gap}, which have an opposite effect on the DMI. By applying a tensile strain to the system, the DMI decreases nearly linearly for stacking 3.

3. Electric field

The FLAPW method in film geometry as implemented in the FLEUR code is used to include the effect of an external electric field as described in Ref. [87]. An out-of-plane electric

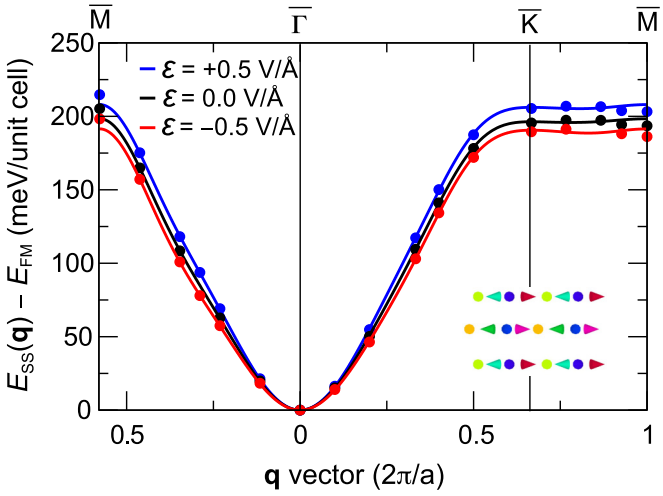

FIG. 7. Energy dispersions of spin spirals propagating in all Fe layers (see inset) of FGT/Ge in the scalar-relativistic approximation, i.e., without SOC, calculated via the FLAPW method along two high-symmetry directions ($\overline{\Gamma KM}$ and $\overline{\Gamma M}$) at electric fields of $\mathcal{E} = +0.5$ V/Å (blue), $\mathcal{E} = 0.0$ V/Å (black), and $\mathcal{E} = -0.5$ V/Å (red). The solid circles represent DFT total energies, and the solid curves are fits to the Heisenberg model (see Table II for exchange constants).

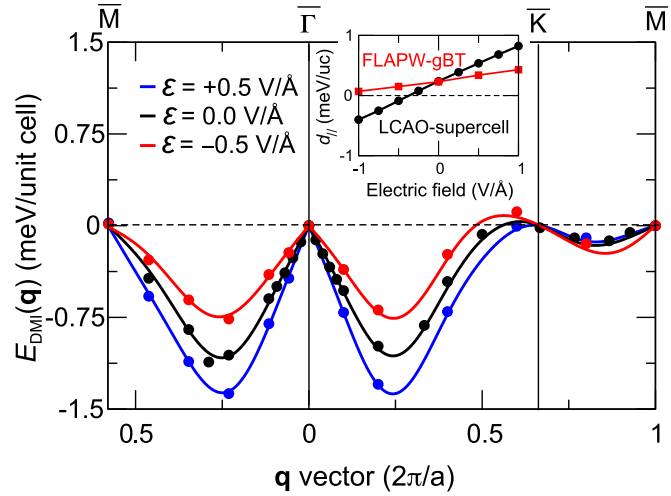

FIG. 8. SOC-induced energy contribution $E_{\mathrm{DMI}}(\mathbf{q})$ to the dispersion of flat cycloidal spin spirals propagating in all Fe layers of FGT/Ge calculated via the FLAPW method along the high-symmetry directions ($\overline{\Gamma KM}$ and $\overline{\Gamma M}$) at $\mathcal{E} = +0.5$ V/Å (blue), $\mathcal{E} = 0.0$ V/Å (black), and $\mathcal{E} = -0.5$ V/Å (red). The solid circles represent DFT data, and the solid curves are fits to the DMI term of the atomistic spin model. The inset shows the DMI constant in the NN approximation for the FGT/Ge heterostructure as a function of the perpendicular electric field, calculated by the LCAO-supercell (black) approach, and the value of the NN DMI constant obtained with the FLAPW-gBT (red) approach (for all values, see Table II). Here, uc means unit cell.

field is defined by adding a charge plate in the vacuum and adding the same amount of opposite charge to FGT/Ge (cf. Fig. 1) to maintain charge neutrality [65,87,88]. We chose electric field values of $\mathcal{E} = \pm 0.5$ V/Å, which can be applied in scanning tunneling microscopy experiments [89] and allow to write and delete isolated magnetic skyrmions in ultrathin transition-metal films as demonstrated experimentally [89] and based on atomistic spin simulations with DFT parameters [65,90]. Note that we use the same sign convention for the electric field as in Refs. [65,90].

We show in Fig. 7 the energy dispersion $E_{\mathrm{ss}}(\mathbf{q})$ of homogeneous flat spin spirals propagating in all Fe layers of FGT/Ge in the scalar-relativistic approximation, i.e., without SOC. Upon including a negative electric field with a strength of $\mathcal{E} = -0.5$ V/Å, the energy rises more slowly at the $\overline{\Gamma}$ point (FM state) than for $\mathcal{E} = 0$, and the energy difference with respect to the AFM state ($\overline{\mathrm{M}}$ point) and Néel state ($\overline{\mathrm{K}}$ point) decreases. For a positive electric field of $\mathcal{E} = +0.5$ V/Å, we observe the opposite effect, i.e., a faster rise and larger energy differences at the high-symmetry points. This field effect is similar to that observed for Fe monolayers on transition-metal surfaces [65].

By fitting the energy dispersions with and without an applied electric field, we obtain the field effect on the exchange constants (see Table II). Note that we treat three Fe atoms as a whole in this spin model, i.e., without explicitly considering the exchange interactions between different Fe pairs. In other words, the definition of J_i is different from the one defined in Sec. III B. Here, the exchange interactions between different Fe pairs are included in an averaged way. We find a nearly linear decrease in the nearest-neighbor exchange constant, J_1, by about 6% upon applying an electric field of 1 V/Å. The exchange constants beyond nearest neighbors are also significantly influenced by the electric field, which shows that the exchange frustration increases for a positive electric field. The effect of the electric field on the exchange interaction can be explained based on its spin-dependent screening at the surface as shown previously for ultrathin 3*d* transition-metal films [65,88].

Figure 8 shows the SOC-induced DMI contributions to the energy dispersion of cycloidal spin spirals in FGT/Ge, $E_{\mathrm{DMI}}(\mathbf{q})$, under an electric field. When an electric field is applied, $E_{\mathrm{DMI}}(\mathbf{q})$ displays the same trend as in zero field, i.e.,

TABLE II. Shell-resolved Heisenberg exchange constants J_i and DMI constants D_i obtained by fitting the energy contribution to spin spirals without and with SOC from DFT calculations using the FLAPW method as presented in Figs. 7 and 8 for three electric field values. A positive (negative) sign of D_i denotes a preference of CW (CCW) rotating cycloidal spin spirals. All values are given in meV/unit cell.

	J_1	J_2	J_3	J_4	J_5	J_6	J_7	J_8	D_1	D_2	D_3	D_4	D_5	D_6	D_7
+0.5 V/Å	23.73	0.16	−1.61	0.48	1.12	−0.28	0.00	−0.15	0.31	0.09	−0.01	−0.01	−0.01	0.00	0.00
0.0 V/Å	22.87	−0.21	−1.78	0.43	1.25	−0.31	0.00	−0.15	0.23	0.10	0.00	0.00	0.00	0.00	0.00
−0.5 V/Å	22.35	−0.62	−1.90	0.38	1.30	−0.37	0.06	−0.17	0.14	0.08	−0.01	−0.01	−0.01	0.00	0.00

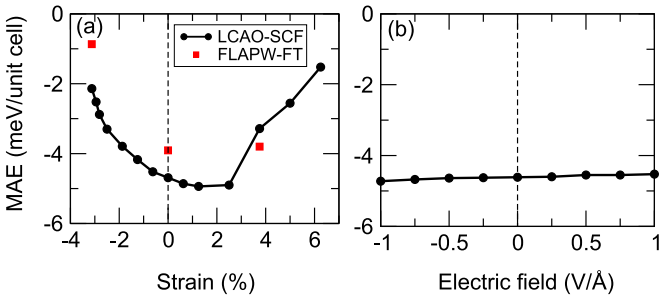

FIG. 9. (a) Strain- and (b) electric-field-dependent MAE in the FGT/Ge heterostructure obtained by the LCAO-SCF (solid black circles) and FLAPW-FT (solid red squares) approaches.

it favors cycloidal spirals with a CW rotational sense, but an electric-field-induced modification in $E_{\mathrm{DMI}}(\mathbf{q})$ is clearly seen. The out-of-plane electric field breaks the inversion symmetry and leads to a drastic change in the nearest-neighbor DMI constant, D_1, which increases and decreases by approximately 40% for $\mathcal{E} = +0.5$ V/Å and $\mathcal{E} = -0.5$ V/Å, respectively (see Table II). Additionally, we find that D_2 remains almost the same while terms beyond D_2 are negligible.

In general, when an electric field is applied from negative to positive, the DMI in FGT/Ge favors less and less a CW rotational sense. This is also reproduced by the LCAO-supercell approach (see inset of Fig. 8), in which we even find a change of sign of the DMI constant at $\mathcal{E} < -0.37$ V/Å. However, quantitatively, we note that LCAO-supercell overestimates the DMI compared with FLAPW-gBT under an electric field. We attribute this quantitative discrepancy to the different implementations of the electric field and basis sets used in the FLAPW-gBT and LCAO-supercell methods.

Note that the electric field effect on the exchange interaction is opposite to that on the DMI with respect to the formation of noncollinear spin states. For $\mathcal{E} < 0$, the energy dispersion without SOC (Fig. 7) rises less quickly, and the exchange frustration increases, which is favorable for the emergence of spin structures such as skyrmions. However, the energy contribution due to DMI (Fig. 8) shows a shallower energy minimum for $\mathcal{E} < 0$, and the nearest-neighbor DMI constant drops accordingly (cf. Table II). This shows that both the effect on the exchange and the effect on the DMI need to be taken into account in order to predict electric-field-assisted formation of noncollinear spin structures in line with previous theoretical studies [65,90]. In contrast, the electric field effect on the magnetocrystalline anisotropy energy is small (see next section).

D. FGT/Ge: Magnetocrystalline anisotropy energy

We define the MAE as the difference in total energies between a configuration in which the magnetization in the ferromagnetic state is in plane (∥) and out of plane (⊥) with respect to the FGT monolayer

$$\mathrm{MAE} = E_{\perp} - E_{\parallel}. \tag{15}$$

In Fig. 9,we plot the MAE in the FGT/Ge heterostructure as a function of strain and electric field. We calculate the MAE using two approaches: (i) The MAE is defined as the energy difference between self-consistently converged total energies including SOC, namely, LCAO-SCF (where SCF refers to self-consistent field); and (ii) the MAE is taken as the band energy difference [also known as the force theorem (FT)] obtained after a one-step diagonalization of the full Hamiltonian including SOC, starting from the well-converged self-consistent scalar relativistic (without SOC) density/potential, namely, FLAPW-FT.

We find that FGT/Ge has a strong perpendicular MAE of more than 4.62 meV (about 1.5 meV/Fe). Interestingly, when a mechanical strain is applied, the MAE can be significantly reduced to 2.08 meV at $\gamma = -3\%$ and 1.44 meV at $\gamma = 6.1\%$, respectively. In general, the two DFT approaches yield a good qualitative agreement concerning the change in the MAE with strain. From the local decomposition of MAE evaluated by the grand-canonical formulation [91,92], we find that Fe1 and Fe3 favor out-of-plane anisotropy while the Fe2 layer favors an in-plane direction of the moments. In contrast, we find that an applied electric field has a much smaller effect on the MAE of FGT/Ge [Fig. 9(b)].

IV. CONCLUSION

In summary, Fe_3GeTe_2/germanene has been investigated as a representative 2D vdW magnetic heterostructure using three current state-of-the-art approaches to map the *ab initio* DFT calculations to an atomistic spin model: (i) the Green's function approach performing infinitesimal rotations, (ii) the spin spiral method employing the generalized Bloch theorem for various $\mathbf{q}$ vectors, and (iii) the supercell approach based on the chirality-dependent total energy difference. We obtain good qualitative agreement for the Heisenberg exchange and Dzyaloshinskii-Moriya interaction in FGT/Ge using these three different approaches. We obtain almost quantitative agreement for the DMI between approaches (ii) and (iii), indicating that the nearest-neighbor approximation is valid in the FGT/Ge heterostructure. Furthermore, we have studied the electronic and magnetic ground states of the FGT/Ge heterostructure under biaxial mechanical strain, stacking, and

TABLE III. Shell-resolved Heisenberg exchange constants, J_i, for ith neighbors for the different Fe-Fe pairs in FGT fitted from the spin spiral DFT calculations via the FLAPW method presented in Fig. 3. All values are given in meV.

	J_1	J_2	J_3	J_4	J_5	J_6	J_7
Fe3-Fe3 (Fe1-Fe1)	−10.21	−0.30	1.28	0.19	−0.28	0.03	0.04
Fe2-Fe2	−2.02	0.50	−0.53	−0.20	−0.01	0.03	−0.38
Fe3-Fe2 (Fe2-Fe1)	16.50	5.42	−1.23	−0.82	1.01	1.11	0.50
Fe3-Fe1	83.47	−6.40	4.13	6.86	−1.08	1.09	1.25

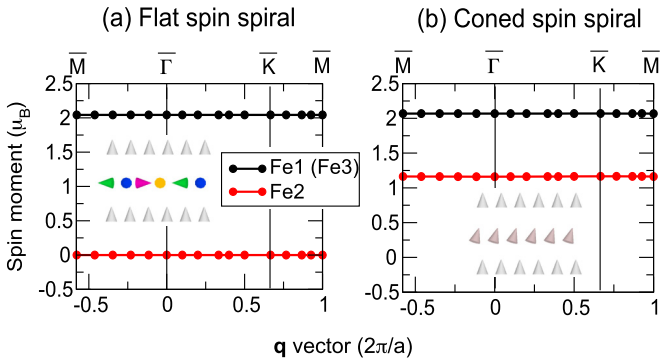

FIG. 10. Magnetic moments of the Fe1 (Fe3) and Fe2 atoms in a freestanding FGT monolayer as a function of the **q** vector for (a) flat ($\theta = \pi/2$) and (b) conical (with a small cone angle of $\theta = \pi/20$) spin spirals calculated via the FLAPW method.

a perpendicular electric field. We have shown that the strength of the DMI can be significantly modified via strain and stacking order, tracing its origin to the geometrical change and hybridization effect. In particular, when a small compressive strain is applied, the DMI is strongly enhanced while the MAE, in contrast, is significantly decreased, which allows the possibility of nanoscale skyrmions at a low magnetic field [58]. On the other hand, an electric field changes the DMI and the exchange constants almost linearly. If we apply a large enough electric field, we also expect a change in the sign of the DMI, i.e., a reversed rotational sense of the favored noncollinear spin structures. The electric field effect on the magnetocrystalline anisotropy is small for the FGT/Ge heterostructure.

ACKNOWLEDGMENTS

This study has been supported through ANR Grant No. ANR-22-CE24-0019. This study has been (partially) supported through the NanoX Grant No. ANR-17-EURE-0009 in the framework of the "Programme des Investissements d'Avenir." S. Haldar, T.D., and S. Heinze gratefully acknowledge financial support from the Deutsche Forschungsgemeinschaft (DFG, German Research Foundation) through SPP2137 "Skyrmionics" (Project No. 462602351). This work was performed using high-performance computing resources from CALMIP (Grant No. 2023-[P21008]). D.L. thanks F. Nickel for valuable discussions. D.L. acknowledges the Alexander von Humboldt Foundation.

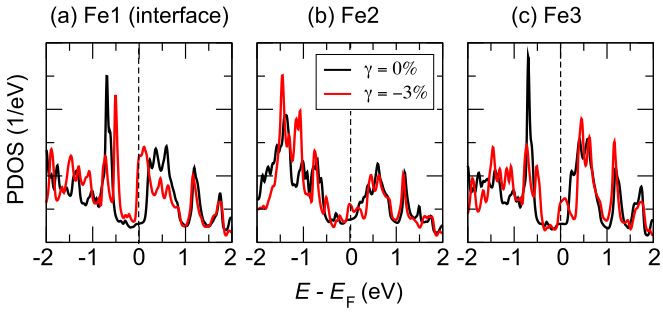

FIG. 11. Calculated spin-averaged PDOS on (a) Fe1, (b) Fe2, and (c) Fe3 atoms in an FGT/Ge bilayer in equilibrium, i.e., $\gamma = 0\%$ (black), and under a compressive strain of $\gamma = -3\%$ (red) obtained by the LCAO-Green approach. The Fermi energy is set to zero.

APPENDIX A: FITTED HEISENBERG EXCHANGE PARAMETERS FOR FREESTANDING FGT

In Table III, we present the fitted parameters up to the seventh-nearest neighbors for freestanding FGT obtained via FLAPW-gBT. Note that in the main text we only benchmarked the NN exchange parameter.

APPENDIX B: QUENCHING OF THE MAGNETIC MOMENT

Spin spirals can be characterized by their reciprocal spin spiral vector **q**, which determines the propagation direction of the spiral. For a rotation axis along the z direction, their magnetization is defined as

$$\mathbf{m}_i = \begin{pmatrix} \cos(\mathbf{q}\cdot\mathbf{R}_i)\sin\theta \\ \sin(\mathbf{q}\cdot\mathbf{R}_i)\sin\theta \\ \cos\theta \end{pmatrix}, \tag{B1}$$

where $\mathbf{R}_i$ is the position of site i and θ is the cone angle. For the special value $\theta = \pi/2$, we obtain flat spin spirals.

We show in Fig. 10 the variation of magnetic moments along **q** vectors for flat [Fig. 10(a)] and conical [Fig. 10(b)] spin spirals for Fe2-Fe2 spin spirals in a freestanding FGT monolayer, where we rotate only the spins of the Fe2 atoms by fixing the other two layers to the FM state. For flat spin spirals [Fig. 10(a)], only the Fe3 and Fe1 layers possess a magnetic moment, while the moments of the Fe2 atom vanish due to symmetry. On the other, for conical spin spirals [Fig. 10(b)], we obtain the expected magnetic moments (close to the FM state) for all three atoms.

APPENDIX C: THE PARTIAL DENSITY OF STATES IN FGT/Ge WITHOUT AND WITH STRAIN

To further show that the mechanism of strong enhancement of the DMI originates mainly from the Fe1-atom-related pairs (see Fig. 5), the partial density of states (PDOS) of Fe atoms in FGT/Ge under strains of $\gamma = -3$ and 0% is analyzed in Fig. 11. The largest difference between the two cases originates from the Fe1 atom, which is located at the interface.

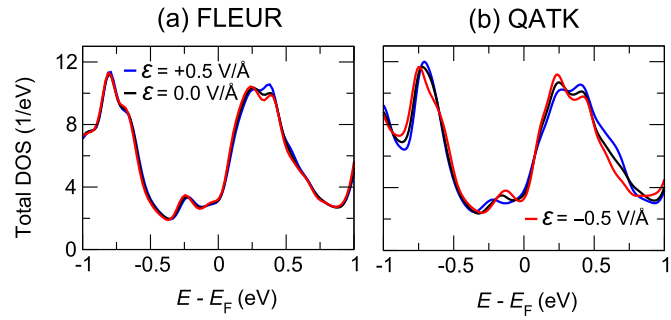

FIG. 12. Total DOS of FGT/Ge obtained via (a) the FLEUR code and (b) QATK at electric fields of $\mathcal{E} = +0.5$ V/Å (blue), $\mathcal{E} = 0.0$ V/Å (black), and $\mathcal{E} = -0.5$ V/Å (red).

APPENDIX D: COMPARISON OF FLEUR AND QATK

We plot in Fig. 12 the total density of states (DOS) for FGT/Ge calculated by the FLEUR code [Fig. 12(a)] and by the QATK code [Fig. 12(b)] at different electric fields. We note that the effect of the electric field on the PDOS is much more pronounced in QATK than in FLEUR, leading to the quantitative difference in the variation of the DMI with electric field observed in the inset of Fig. 8.

[1] A. Bogdanov and D. Yablonskii, Thermodynamically stable "vortices" in magnetically ordered crystals. The mixed state of magnets, Zh. Eksp. Teor. Fiz. **95**, 178 (1989).

[2] A. Fert, V. Cros, and J. Sampaio, Skyrmions on the track, Nat. Nanotechnol. **8**, 152 (2013).

[3] S. Luo, M. Song, X. Li, Y. Zhang, J. Hong, X. Yang, X. Zou, N. Xu, and L. You, Reconfigurable skyrmion logic gates, Nano Lett. **18**, 1180 (2018).

[4] K. Song, J. Jeong, B. Pan, X. Zhang, J. Xia, S. Cha, T. Park, K. Kim, S. Finizio, J. Raabe, J. Chang, Y. Zhou, W. Zhao, W. Kang, H. Ju, and S. Woo, Skyrmion-based artificial synapses for neuromorphic computing, Nat. Electron. **3**, 148 (2020).

[5] C. Psaroudaki and C. Panagopoulos, Skyrmion Qubits: A New Class of Quantum Logic Elements Based on Nanoscale Magnetization, Phys. Rev. Lett. **127**, 067201 (2021).

[6] T. Moriya, Anisotropic Superexchange Interaction and Weak Ferromagnetism, Phys. Rev. **120**, 91 (1960).

[7] I. E. Dzialoshinskii, Thermodynamic theory of "weak" ferromagnetism in antiferromagnetic substances, Sov. Phys. JETP **5**, 1259 (1957).

[8] A. Fert and P. M. Levy, Role of Anisotropic Exchange Interactions in Determining the Properties of Spin-Glasses, Phys. Rev. Lett. **44**, 1538 (1980).

[9] M. Bode, M. Heide, K. Von Bergmann, P. Ferriani, S. Heinze, G. Bihlmayer, A. Kubetzka, O. Pietzsch, S. Blügel, and R. Wiesendanger, Chiral magnetic order at surfaces driven by inversion asymmetry, Nature (London) **447**, 190 (2007).

[10] S. Mühlbauer, B. Binz, F. Jonietz, C. Pfleiderer, A. Rosch, A. Neubauer, R. Georgii, and P. Boni, Skyrmion lattice in a chiral magnet, Science **323**, 915 (2009).

[11] X. Yu, Y. Onose, N. Kanazawa, J. Park, J. Han, Y. Matsui, N. Nagaosa, and Y. Tokura, Real-space observation of a two-dimensional skyrmion crystal, Nature (London) **465**, 901 (2010).

[12] S. Heinze, K. Von Bergmann, M. Menzel, J. Brede, A. Kubetzka, R. Wiesendanger, G. Bihlmayer, and S. Blügel, Spontaneous atomic-scale magnetic skyrmion lattice in two dimensions, Nat. Phys. **7**, 713 (2011).

[13] N. Romming, C. Hanneken, M. Menzel, J. Bickel, B. Wolter, K. von Bergmann, A. Kubetzka, and R. Wiesendanger, Writing and deleting single magnetic skyrmions, Science **341**, 636 (2013).

[14] M. Hervé, B. Dupé, R. Lopes, M. Böttcher, M. D. Martins, T. Balashov, L. Gerhard, J. Sinova, and W. Wulfhekel, Stabilizing spin spirals and isolated skyrmions at low magnetic field exploiting vanishing magnetic anisotropy, Nat. Commun. **9**, 1015 (2018).

[15] S. Meyer, M. Perini, S. von Malottki, A. Kubetzka, R. Wiesendanger, K. von Bergmann, and S. Heinze, Isolated zero field sub-10 nm skyrmions in ultrathin Co films, Nat. Commun. **10**, 3823 (2019).

[16] C. Moreau-Luchaire, C. Moutafis, N. Reyren, J. Sampaio, C. Vaz, N. Van Horne, K. Bouzehouane, K. Garcia, C. Deranlot, P. Warnicke, P. Wohlhüter, J.-M. George, M. Weigand, J. Raabe, V. Cros, and A. Fert, Additive interfacial chiral interaction in multilayers for stabilization of small individual skyrmions at room temperature, Nat. Nanotechnol. **11**, 444 (2016).

[17] O. Boulle, J. Vogel, H. Yang, S. Pizzini, D. de Souza Chaves, A. Locatelli, T. Menteş, A. Sala, L. Buda-Prejbeanu, O. Klein, M. Belmeguenai, Y. Roussigné, A. Stashkevich, S. M. Chérif, L. Aballe, M. Foerster, M. Chshiev, S. Auffret, I. M. Miron, and G. Gaudin, Room-temperature chiral magnetic skyrmions in ultrathin magnetic nanostructures, Nat. Nanotechnol. **11**, 449 (2016).

[18] S. Woo, K. Litzius, B. Krüger, M. Im, L. Caretta, K. Richter, M. Mann, A. Krone, R. M. Reeve, M. Weigand, P. Agrawal, I. Lemesh, M.-A. Mawass, P. Fischer, M. Kläui, and G. S. D. Beach, Observation of room-temperature magnetic skyrmions and their current-driven dynamics in ultrathin metallic ferromagnets, Nat. Mater. **15**, 501 (2016).

[19] A. Soumyanarayanan, M. Raju, A. Gonzalez Oyarce, A. Tan, M. Im, A. Petrovic, P. Ho, K. Khoo, M. Tran, C. Gan, F. Ernult, and C. Panagopoulos, Tunable room-temperature magnetic skyrmions in Ir/Fe/Co/Pt multilayers, Nat. Mater. **16**, 898 (2017).

[20] L. Caretta, M. Mann, F. Büttner, K. Ueda, B. Pfau, C. Günther, P. Hessing, A. Churikova, C. Klose, M. Schneider, D. Engel, C. Marcus, D. Bono, K. Bagschik, S. Eisebitt, and G. S. D. Beach, Fast current-driven domain walls and small skyrmions in a compensated ferrimagnet, Nat. Nanotechnol. **13**, 1154 (2018).

[21] W. Legrand, D. Maccariello, F. Ajejas, S. Collin, A. Vecchiola, K. Bouzehouane, N. Reyren, V. Cros, and A. Fert, Room-temperature stabilization of antiferromagnetic skyrmions in synthetic antiferromagnets, Nat. Mater. **19**, 34 (2020).

[22] C. Gong, L. Li, Z. Li, H. Ji, A. Stern, Y. Xia, T. Cao, W. Bao, C. Wang, Y. Wang, Z. Q. Qiu, R. J. Cava, S. G. Louie, J. Xia, and X. Zhang, Discovery of intrinsic ferromagnetism in two-dimensional van der Waals crystals, Nature (London) **546**, 265 (2017).

[23] B. Huang, G. Clark, E. Navarro-Moratalla, D. Klein, R. Cheng, K. Seyler, D. Zhong, E. Schmidgall, M. McGuire, D. Cobden, W. Yao, D. Xiao, P. Jarillo-Herrero, and X. Xu, Layer-dependent ferromagnetism in a van der Waals crystal down to the monolayer limit, Nature (London) **546**, 270 (2017).

[24] Y. Deng, Y. Yu, Y. Song, J. Zhang, N. Wang, Z. Sun, Y. Yi, Y. Wu, S. Wu, J. Zhu, J. Wang, X. H. Chen, and Y. Zhang, Gate-tunable room-temperature ferromagnetism in two-dimensional Fe_3GeTe_2, Nature (London) **563**, 94 (2018).

[25] Y. Wu, S. Zhang, J. Zhang, W. Wang, Y. Zhu, J. Hu, G. Yin, K. Wong, C. Fang, C. Wan, X. Han, Q. Shao, T. Taniguchi, K. Watanabe, J. Zang, Z. Mao, X. Zhang, and K. L. Wang, Néel-type skyrmion in WTe_2/Fe_3GeTe_2 van der Waals heterostructure, Nat. Commun. **11**, 3860 (2020).

[26] M. Yang, Q. Li, R. Chopdekar, R. Dhall, J. Turner, J. Carlström, C. Ophus, C. Klewe, P. Shafer, A. N'Diaye, J. W. Choi, G. Chen, Y. Z. Wu, C. Hwang, F. Wang, and Z. Q. Qiu, Creation of skyrmions in van der Waals ferromagnet Fe_3GeTe_2 on $(Co/Pd)_n$ superlattice, Sci. Adv. **6**, eabb5157 (2020).

[27] Y. Wu, B. Francisco, Z. Chen, W. Wang, Y. Zhang, C. Wan, X. Han, H. Chi, Y. Hou, A. Lodesani, G. Yin, K. Liu, Y. Cui, K. Wang, and J. Moodera, A van der Waals interface hosting two groups of magnetic skyrmions, Adv. Mater. **34**, 2110583 (2022).

[28] H.-H. Yang, N. Bansal, P. Rüßmann, M. Hoffmann, L. Zhang, D. Go, Q. Li, A.-A. Haghighirad, K. Sen, S. Blügel, M. L. Tacon, Y. Mokrousov, and W. Wulfhekel, Magnetic domain walls of the van der Waals material Fe_3GeTe_2, 2D Mater. **9**, 025022 (2022).

[29] M. Costa, N. M. R. Peres, J. Fernández-Rossier, and A. T. Costa, Nonreciprocal magnons in a two-dimensional crystal with out-of-plane magnetization, Phys. Rev. B **102**, 014450 (2020).

[30] J. Liang, W. Wang, H. Du, A. Hallal, K. Garcia, M. Chshiev, A. Fert, and H. Yang, Very large Dzyaloshinskii-Moriya interaction in two-dimensional Janus manganese dichalcogenides and its application to realize skyrmion states, Phys. Rev. B **101**, 184401 (2020).

[31] J. Yuan, Y. Yang, Y. Cai, Y. Wu, Y. Chen, X. Yan, and L. Shen, Intrinsic skyrmions in monolayer Janus magnets, Phys. Rev. B **101**, 094420 (2020).

[32] C. Xu, J. Feng, S. Prokhorenko, Y. Nahas, H. Xiang, and L. Bellaiche, Topological spin texture in janus monolayers of the chromium trihalides $Cr(I, X)_3$, Phys. Rev. B **101**, 060404(R) (2020).

[33] Q. Cui, J. Liang, Z. Shao, P. Cui, and H. Yang, Strain-tunable ferromagnetism and chiral spin textures in two-dimensional Janus chromium dichalcogenides, Phys. Rev. B **102**, 094425 (2020).

[34] J. Jiang, X. Liu, R. Li, and W. Mi, Topological spin textures in a two-dimensional $MnBi_2(Se, Te)_4$ Janus material, Appl. Phys. Lett. **119**, 072401 (2021).

[35] Z. Shen, C. Song, Y. Xue, Z. Wu, J. Wang, and Z. Zhong, Strain-tunable Dzyaloshinskii-Moriya interaction and skyrmions in two-dimensional Janus $Cr_2X_3Y_3(X, Y = \mathrm{Cl, Br, I}, X \neq Y)$ trihalide monolayers, Phys. Rev. B **106**, 094403 (2022).

[36] T. E. Park, L. Peng, J. Liang, A. Hallal, F. S. Yasin, X. Zhang, K. M. Song, S. J. Kim, K. Kim, M. Weigand, G. Schütz, S. Finizio, J. Raabe, K. Garcia, J. Xia, Y. Zhou, M. Ezawa, X. Liu, J. Chang, H. C. Koo *et al.*, Néel-type skyrmions and their current-induced motion in van der Waals ferromagnet-based heterostructures, Phys. Rev. B **103**, 104410 (2021).

[37] W. Sun, W. Wang, H. Li, G. Zhang, D. Chen, J. Wang, and Z. Cheng, Controlling bimerons as skyrmion analogues by ferroelectric polarization in 2D van der Waals multiferroic heterostructures, Nat. Commun. **11**, 5930 (2020).

[38] Q. Tong, F. Liu, J. Xiao, and W. Yao, Skyrmions in the moiré of van der Waals 2D magnets, Nano Lett. **18**, 7194 (2018).

[39] D. Amoroso, P. Barone, and S. Picozzi, Spontaneous skyrmionic lattice from anisotropic symmetric exchange in a Ni-halide monolayer, Nat. Commun. **11**, 5784 (2020).

[40] C. Gong and X. Zhang, Two-dimensional magnetic crystals and emergent heterostructure devices, Science **363**, eaav4450 (2019).

[41] X. Jiang, Q. Liu, J. Xing, N. Liu, Y. Guo, Z. Liu, and J. Zhao, Recent progress on 2D magnets: Fundamental mechanism, structural design and modification, Appl. Phys. Rev. **8**, 031305 (2021).

[42] P. Ferriani, K. von Bergmann, E. Y. Vedmedenko, S. Heinze, M. Bode, M. Heide, G. Bihlmayer, S. Blügel, and R. Wiesendanger, Atomic-Scale Spin Spiral with a Unique Rotational Sense: Mn Monolayer on W(001), Phys. Rev. Lett. **101**, 027201 (2008).

[43] M. Heide, G. Bihlmayer, and S. Blügel, Describing Dzyaloshinskii-Moriya spirals from first principles, Phys. B (Amsterdam) **404**, 2678 (2009).

[44] R. Yanes, J. Jackson, L. Udvardi, L. Szunyogh, and U. Nowak, Exchange Bias Driven by Dzyaloshinskii-Moriya Interactions, Phys. Rev. Lett. **111**, 217202 (2013).

[45] V. Kashid, T. Schena, B. Zimmermann, Y. Mokrousov, S. Blügel, V. Shah, and H. G. Salunke, Dzyaloshinskii-Moriya interaction and chiral magnetism in $3d - 5d$ zigzag chains: Tight-binding model and *ab initio* calculations, Phys. Rev. B **90**, 054412 (2014).

[46] B. Zimmermann, M. Heide, G. Bihlmayer, and S. Blügel, First-principles analysis of a homochiral cycloidal magnetic structure in a monolayer Cr on W(110), Phys. Rev. B **90**, 115427 (2014).

[47] B. Dupé, M. Hoffmann, C. Paillard, and S. Heinze, Tailoring magnetic skyrmions in ultra-thin transition metal films, Nat. Commun. **5**, 4030 (2014).

[48] E. Simon, K. Palotás, L. Rózsa, L. Udvardi, and L. Szunyogh, Formation of magnetic skyrmions with tunable properties in PdFe bilayer deposited on Ir(111), Phys. Rev. B **90**, 094410 (2014).

[49] H. Yang, A. Thiaville, S. Rohart, A. Fert, and M. Chshiev, Anatomy of Dzyaloshinskii-Moriya Interaction at Co/Pt Interfaces, Phys. Rev. Lett. **115**, 267210 (2015).

[50] G. J. Vida, E. Simon, L. Rózsa, K. Palotás, and L. Szunyogh, Domain-wall profiles in $Co/Ir_n/Pt(111)$ ultrathin films: Influence of the Dzyaloshinskii-Moriya interaction, Phys. Rev. B **94**, 214422 (2016).

[51] K. Yamamoto, A. Pradipto, K. Nawa, T. Akiyama, T. Ito, T. Ono, and K. Nakamura, Interfacial Dzyaloshinskii-Moriya interaction and orbital magnetic moments of metallic multilayer films, AIP Adv. **7**, 056302 (2017).

[52] E. Simon, L. Rózsa, K. Palotás, and L. Szunyogh, Magnetism of a Co monolayer on Pt(111) capped by overlayers of $5d$ elements: A spin-model study, Phys. Rev. B **97**, 134405 (2018).

[53] P. Jadaun, L. Register, and S. Banerjee, The microscopic origin of DMI in magnetic bilayers and prediction of giant DMI in new bilayers, npj Comput. Mater. **6**, 88 (2020).

[54] B. Zimmermann, G. Bihlmayer, M. Böttcher, M. Bouhassoune, S. Lounis, J. Sinova, S. Heinze, S. Blügel, and B. Dupé, Comparison of first-principles methods to extract magnetic parameters in ultrathin films: Co/Pt(111), Phys. Rev. B **99**, 214426 (2019).

[55] A. Liechtenstein, M. Katsnelson, V. Antropov, and V. Gubanov, Local spin density functional approach to the theory of exchange interactions in ferromagnetic metals and alloys, J. Magn. Magn. Mater. **67**, 65 (1987).

[56] L. M. Sandratskii, Energy band structure calculations for crystals with spiral magnetic structure, Phys. Status Solidi B **136**, 167 (1986).

[57] P. Kurz, F. Förster, L. Nordström, G. Bihlmayer, and S. Blügel, *Ab initio* treatment of noncollinear magnets with the full-potential linearized augmented plane wave method, Phys. Rev. B **69**, 024415 (2004).

[58] D. Li, S. Haldar, and S. Heinze, Strain-driven zero-field near-10 nm skyrmions in two-dimensional van der Waals heterostructures, Nano Lett. **22**, 7706 (2022).

[59] A. Szilva, M. Costa, A. Bergman, L. Szunyogh, L. Nordström, and O. Eriksson, Interatomic Exchange Interactions for Finite-Temperature Magnetism and Nonequilibrium Spin Dynamics, Phys. Rev. Lett. **111**, 127204 (2013).

[60] S. Smidstrup, T. Markussen, P. Vancraeyveld, J. Wellendorff, J. Schneider, T. Gunst, B. Verstichel, D. Stradi, P. Khomyakov, U. Vej-Hansen, M.-E. Lee, S. T. Chill, F. Rasmussen, G. Penazzi, F. Corsetti, A. Ojanperä, K. Jensen, M. L. N. Palsgaard, U. Martinez, A. Blom *et al.*, QuantumATK: an integrated platform of electronic and atomic-scale modelling tools, J. Phys.: Condens. Matter **32**, 015901 (2020).

[61] https://www.flapw.de/MaX-6.0/.

[62] H. Xiang, C. Lee, H.-J. Koo, X. Gong, and M.-H. Whangbo, Magnetic properties and energy-mapping analysis, Dalton Trans. **42**, 823 (2013).

[63] H. Yu, C. Xu, X. Li, F. Lou, L. Bellaiche, Z. Hu, X. Gong, and H. Xiang, Complex spin Hamiltonian represented by an artificial neural network, Phys. Rev. B **105**, 174422 (2022).

[64] L. Oroszlány, J. Ferrer, A. Deák, L. Udvardi, and L. Szunyogh, Exchange interactions from a nonorthogonal basis set: From bulk ferromagnets to the magnetism in low-dimensional graphene systems, Phys. Rev. B **99**, 224412 (2019).

[65] S. Paul and S. Heinze, Electric-field driven stability control of skyrmions in an ultrathin transition-metal film, npj Comput. Mater. **8**, 105 (2022).

[66] W. Du, K. Dou, Z. He, Y. Dai, B. Huang, and Y. Ma, Spontaneous magnetic skyrmions in single-layer $CrInX_3$ (X = Te, Se), Nano Lett. **22**, 3440 (2022).

[67] J. M. J. Lopes, D. Czubak, E. Zallo, A. I. Figueroa, C. Guillemard, M. Valvidares, J. Rubio-Zuazo, J. López-Sanchéz, S. O. Valenzuela, M. Hanke, and M. Ramsteiner, Large-area van der Waals epitaxy and magnetic characterization of Fe_3GeTe_2 films on graphene, 2D Mater. **8**, 041001 (2021).

[68] Z. Wang, D. Sapkota, T. Taniguchi, K. Watanabe, D. Mandrus, and A. F. Morpurgo, Tunneling spin valves based on Fe_3GeTe_2/hBN/Fe_3GeTe_2 van der Waals heterostructures, Nano Lett. **18**, 4303 (2018).

[69] H. Deiseroth, K. Aleksandrov, C. Reiner, L. Kienle, and R. Kremer, Fe_3GeTe_2 and Ni_3GeTe_2 – two new layered transition-metal compounds: Crystal structures, HRTEM investigations, and magnetic and electrical properties, Eur. J. Inorg. Chem. **2006**, 1561 (2006).

[70] B. Chen, J. Yang, H. Wang, M. Imai, H. Ohta, C. Michioka, K. Yoshimura, and M. Fang, Magnetic properties of layered itinerant electron ferromagnet Fe_3GeTe_2, J. Phys. Soc. Jpn. **82**, 124711 (2013).

[71] S. Grimme, J. Antony, S. Ehrlich, and H. Krieg, A consistent and accurate *ab initio* parametrization of density functional dispersion correction (DFT-D) for the 94 elements H-Pu, J. Chem. Phys. **132**, 154104 (2010).

[72] H. L. Zhuang, P. R. C. Kent, and R. G. Hennig, Strong anisotropy and magnetostriction in the two-dimensional stoner ferromagnet Fe_3GeTe_2, Phys. Rev. B **93**, 134407 (2016).

[73] S. Ghosh, S. Ershadrad, V. Borisov, and B. Sanyal, Unraveling effects of electron correlation in two-dimensional Fe_nGeTe_2 ($n = 3, 4, 5$) by dynamical mean field theory, arXiv:2212.08552.

[74] J. He, S. Li, A. Bandyopadhyay, and T. Frauenheim, Unravelling photoinduced interlayer spin transfer dynamics in two-dimensional nonmagnetic-ferromagnetic van der Waals heterostructures, Nano Lett. **21**, 3237 (2021).

[75] A. Leonov and M. Mostovoy, Multiply periodic states and isolated skyrmions in an anisotropic frustrated magnet, Nat. Commun. **6**, 8275 (2015).

[76] S. von Malottki, B. Dupé, P. Bessarab, A. Delin, and S. Heinze, Enhanced skyrmion stability due to exchange frustration, Sci. Rep. **7**, 12299 (2017).

[77] Y. Zhang, C. Xu, P. Chen, Y. Nahas, S. Prokhorenko, and L. Bellaiche, Emergence of skyrmionium in a two-dimensional $CrGe(Se, Te)_3$ Janus monolayer, Phys. Rev. B **102**, 241107(R) (2020).

[78] S. Rijal, C. Xu, and L. Bellaiche, Designing frustration in two-dimensional magnetic systems via the application of uniaxial strain, Phys. Rev. B **103**, 014442 (2021).

[79] M. Zhu, Y. You, G. Xu, J. Tang, Y. Gong, and F. Xu, Strain modulation of magnetic coupling in the metallic van der Waals magnet Fe_3GeTe_2, Intermetallics **131**, 107085 (2021).

[80] C. Xu, X. Li, P. Chen, Y. Zhang, H. Xiang, and L. Bellaiche, Assembling diverse skyrmionic phases in Fe_3GeTe_2 monolayer, Adv. Mater. **34**, 2107779 (2022).

[81] S. Paul, S. Haldar, S. von Malottki, and S. Heinze, Role of higher-order exchange interactions for skyrmion stability, Nat. Commun. **11**, 4756 (2020).

[82] Z. X. Shen, X. Bo, K. Cao, X. Wan, and L. He, Magnetic ground state and electron-doping tuning of Curie temperature in Fe_3GeTe_2: First-principles studies, Phys. Rev. B **103**, 085102 (2021).

[83] S. Laref, K. W. Kim, and A. Manchon, Elusive Dzyaloshinskii-Moriya interaction in monolayer Fe_3GeTe_2, Phys. Rev. B **102**, 060402(R) (2020).

[84] X. Hu, Y. Zhao, X. Shen, A. Krasheninnikov, Z. Chen, and L. Sun, Enhanced ferromagnetism and tunable magnetism in Fe_3GeTe_2 monolayer by strain engineering, ACS Appl. Mater. Interfaces **12**, 26367 (2020).

[85] K. Huang, D. Shao, and E. Tsymbal, Ferroelectric control of magnetic skyrmions in two-dimensional van der Waals heterostructures, Nano Lett. **22**, 3349 (2022).

[86] X. He, N. Helbig, M. Verstraete, and E. Bousquet, TB2J: A python package for computing magnetic interaction parameters, Comput. Phys. Commun. **264**, 107938 (2021).

[87] M. Weinert, G. Schneider, R. Podloucky, and J. Redinger, FLAPW: Applications and implementations, J. Phys.: Condens. Matter **21**, 084201 (2009).

[88] M. Oba, K. Nakamura, T. Akiyama, T. Ito, M. Weinert, and A. J. Freeman, Electric-Field-Induced Modification of the Magnon Energy, Exchange Interaction, and Curie Temperature of Transition-Metal Thin Films, Phys. Rev. Lett. **114**, 107202 (2015).

[89] P. Hsu, A. Kubetzka, A. Finco, N. Romming, K. Von Bergmann, and R. Wiesendanger, Electric-field-driven switching of individual magnetic skyrmions, Nat. Nanotechnol. **12**, 123 (2017).

[90] M. A. Goerzen, S. von Malottki, G. J. Kwiatkowski, P. F. Bessarab, and S. Heinze, Atomistic spin simulations of electric-field-assisted nucleation and annihilation of magnetic skyrmions in Pd/Fe/Ir(111), Phys. Rev. B **105**, 214435 (2022).

[91] D. Li, A. Smogunov, C. Barreteau, F. Ducastelle, and D. Spanjaard, Magnetocrystalline anisotropy energy of Fe(001) and Fe(110) slabs and nanoclusters: A detailed local analysis within a tight-binding model, Phys. Rev. B **88**, 214413 (2013).

[92] D. Li, C. Barreteau, M. R. Castell, F. Silly, and A. Smogunov, Out- versus in-plane magnetic anisotropy of free Fe and Co nanocrystals: Tight-binding and first-principles studies, Phys. Rev. B **90**, 205409 (2014).